Effect of laser polishing on the microstructure and mechanical properties of stainless steel 316L fabricated by laser powder bed fusion

Lan Chen[a,b], Brodan Richter[b], Xinzhou Zhang[a,b], Kaila B. Bertsch[d], Dan J. Thoma[c], Frank E. Pfefferkorn[b,*]

[a] School of Mechanical Engineering, Jiangsu University, Zhenjiang, 212013, China

[b] Department of Mechanical Engineering, University of Wisconsin–Madison, Madison, WI, 53706 USA

[c] Department of Materials Science & Engineering, University of Wisconsin–Madison, Madison, WI, 53706 USA

[d] Lawrence Livermore National Laboratory, Materials Science Division, Livermore, CA, 94550 USA

[*] Corresponding author: frank.pfefferkorn@wisc.edu

Abstract: While metal additive manufacturing has seen significant growth in recent years, the surfaces produced often need post-processing to improve surface finish, mitigate residual stresses, and remove surface-connected porosity. Laser polishing, by means of remelting a thin layer of the surface, is one post-processing method being investigated for surface finish improvements and other surface enhancements. In this work, the surface morphology and microstructure of laser powder bed fused (L-PBF) stainless-steel 316L (316L) before and after laser polishing are characterized by optical microscopy (OM), scanning electron microscopy (SEM), electron back-scatter diffraction (EBSD), and transmission electron microscopy (TEM). In addition, the cross-sectional microhardness of the samples is measured and reported. Additionally, the as-built and laser-polished sample's tensile properties are characterized using uniaxial tension tests. The results indicate that the surface roughness of as-built 316L (Sa = 4.84 μm) can be substantially reduced through laser polishing (Sa = 0.65 μm). After laser polishing, the average grain diameter is reduced and the proportion of low angle grain boundaries (2°~5°) is increased in the L-PBF 316L. The maximum sub-surface hardness reaches 262 HV, and both the tensile strength and ductility of 316L are increased after laser polishing. This enhancement is attributed to thermal cycling stresses, grain refinement, the elimination of surface defects, and dislocation strengthening after laser polishing.

Keywords: Laser polishing; Laser powder bed fusion; Stainless steel; Mechanical property; Microstructure

1. Introduction

Laser powder bed fusion (L-PBF) is one promising technology in the quickly growing field of metal additive manufacturing (AM). L-PBF utilizes a high-energy laser beam to melt metal powder and produce complex three-dimensional parts in a layer-by-layer process that builds parts from bottom to top [1-3]. This manufacturing process does not require any tooling die and is not limited by the complexity of the shape of the part. It has broad application prospects, specifically in the biomedical and aerospace industries [4-6]. L-PBF provides many advantages over traditional manufacturing techniques, but still has drawbacks that limit its widespread use for high-performance parts. Since L-PBF is a solidification-based process, it is prone to unmelted powder, voids, cracks, variable grain size, and other defects [7, 8]. Some surface defects, such as unmelted powder and physical ripples can significantly affect the surface quality and mechanical properties of the as-built part [9].

Compared to polishing by mechanical material removal, laser polishing by remelting provides an adjustable polishing velocity, no chemical contamination from polishing media, and is a non-contact process without tool wear or other polishing-media consumables [10-12]. Shielding gas to minimize oxidation may be a consumable in some applications of laser polishing. When the laser interacts with the surface of the metallic material, it can quickly polish and consolidate the surface due to fluid forces within the melt pool. For complex metal surfaces, laser polishing can also achieve micron-scale and selective polishing quickly. Laser polishing is also suitable for low-hardness metallic material that may be difficult to polish using conventional methods. Due to these advantages, this technology is expected to supplement or potentially replace traditional polishing methods in some application areas [13-15].

Laser polishing by surface remelting has been demonstrated to work for a variety of materials built using L-PBF, including, but not limited to, titanium, cobalt, aluminum, and steel alloys [16-19]. Bhaduri et al. [16] investigated the influence of laser fluence and pulse overlap on surface roughness of L-PBF processed 316L surfaces. The initial surface roughness *Sa* (arithmetical mean height) was improved by 90 % from the as-received value of $Sa = 2.41$ μm at the optimized polishing parameters. Rosa et al. [17] post-processed L-PBF 316L samples using multiple laser polishing parameter sets. After five passes, the surface roughness (*Sa*) was reduced to 0.79 μm with a reduction of 96 %. Yasa and Kruth [18] used

a continuous wave Nd:YAG laser to polish L-PBF processed 316L parts. They studied the effect of scan line spacing, laser power, and velocity on the surface roughness of parts and found that the average roughness was reduced by approximately 70 %. Recent research by Lan et al. [20] demonstrated that laser polishing could improve the corrosion resistance of L-PBF processed 316L, which was attributed to the reduction of surface roughness and refined grains. Although many studies have shown that laser polishing can reduce the surface roughness and improve the mechanical properties of L-PBF processed parts, there are various open questions about how the laser polishing affects the mechanical properties of the final part. The failure of a part can often start from the surface layer, and the performance of a product, especially in regards to its reliability and durability, depends to a large extent on the surface quality of the part [19]. As with traditionally manufactured parts, the properties of L-PBF processed parts depend not only on the surface morphology but also on the microstructure. As the laser polishing process causes the surface to melt and resolidify numerous times, it is expected to affect the microstructure of the melted material. Those changes in microstructure could have a significant effect on the performance of the part. Therefore, understanding the impact that laser polishing has on the microstructural evolution of L-PBF processed parts is critical for understanding the final part's performance.

In this study, laser polishing was employed as a post-treatment to improve the mechanical properties of 316L prepared by L-PBF. The changes of surface morphology, microstructure, and tensile properties before and after laser polishing were investigated. Additionally, the cross-sectional microhardness of all samples was measured. This paper aims to study the relationship between the process-microstructure-properties of laser polishing L-PBF processed 316L. This work provides an insight into laser polishing of 316L parts fabricated by L-PBF and the effect the process can have on those part's mechanical performance.

2. Materials and methods

2.1. Sample production

In this study, 316L samples were fabricated on a stainless-steel 316L substrate using a powder-bed

fusion process (EOS, M290, Germany). Table 1 shows the actual chemical composition of the 316L measured from as-built samples. The measurements were made using combustion infrared detection (for C and Si), inert gas fusion (for O and N), and direct current plasma emission spectroscopy (others). In the L-PBF process, the laser power, layer thickness, and the scan velocity were 195 W, 0.02 mm and 1083 mm/s, respectively. The building direction (BD) was perpendicular to the tensile load direction. The scanning strategy used a 67° rotation between subsequent layers. In order to do preliminary experiments for final experimental parameter selection and for microstructure measurements, various test coupons (with nominal dimensions of 20 × 20 × 5 mm^3) were printed (Fig. 1(a)). In addition, samples with nominal dimensions of 49 × 10 × 5 mm^3 (Fig. 1(a)), were printed alongside the test coupons, and subsequently machined (HAAS, TM1, USA) into tensile samples. The tensile samples (Fig. 1(b)), which were nominally 5 mm thick with a gage length of 25 mm, were cut from the 49 × 10 × 5 mm^3 samples [21]. The dimensions of the tensile samples are based on ASTM E8 and ASTM E345-6 with a reduced grip length to allow all of the samples to be printed in a single build. The samples were not heat-treated or stress relieved before being characterized and tensile tested, in order to test the as-built performance.

Table 1. Chemical composition of SS316L measured from as-built samples. All values are in wt%.

Element	Cr	Ni	Mo	C	Mn	Cu	P	S
	18.390	13.940	2.860	0.004	1.470	0.002	0.017	0.004
Element	Si	N	O	H	Co	Al	Fe	
	0.300	0.065	0.043	0.00008	0.0036	0.002	Bal.	

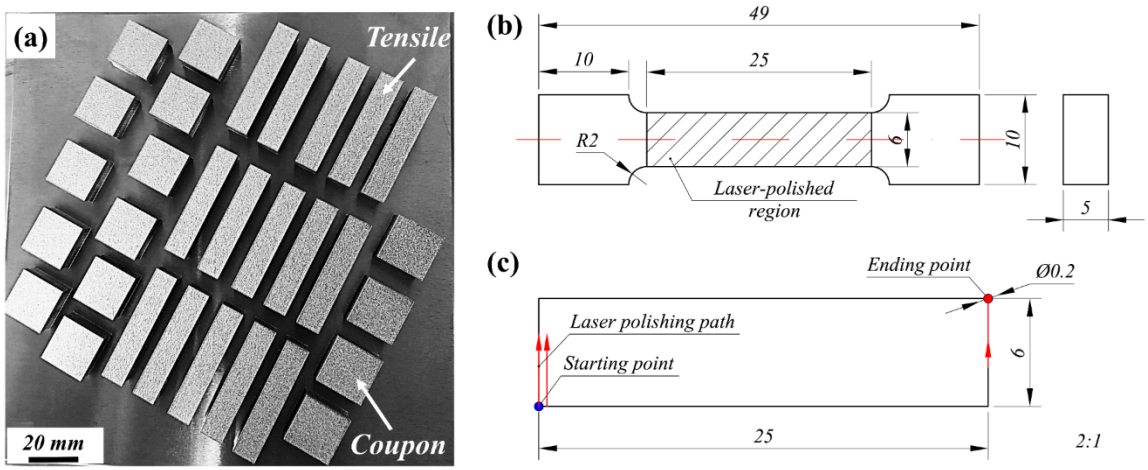

Fig. 1. (a) Two different sizes of L-PBF processed samples; (b) the dimensions of the tensile samples; and (c) partial enlargement drawing of laser-polished region showing the starting point, the laser polishing scanning path and the ending point (distances are given in mm).

2.2. Laser polishing experiments

A schematic of the laser-polishing system is shown in Fig. 2(a). The scanning head (SCANLAB, hurrySCAN II 14, Germany) is used to scan at high speed in a two-dimensional horizontal plane. The position of the sample surface and corresponding laser-beam diameter is controlled by manually adjusting the Z-platform with 0.127 mm steps in the vertical direction. In this study, a 1070 nm, 200 W fiber laser (SPI lasers, Model SP-200C-W-S6-A-B, Germany) was used. The schematic diagram of the remelting mechanism of laser polishing is shown in Fig. 2(b). Laser polishing is the process of melting and re-solidifying a thin layer of the surface. The molten material flows due to surface tension to fill the surface depression, resulting in a final, smooth surface. During the laser-polishing process, the thickness of the molten layer is generally on the micrometer scale [22, 23]. Three different regions are found inside the laser-polished part, namely the melting zone (MZ), the heat affected zone (HAZ), and the base material (BM) [24].

Laser-polishing tests were carried out on the top surface of 20 × 20 × 5 mm^3 cuboids of 316L, one of which is referred to as “coupon” in Fig. 1(a). Fifteen tensile samples were prepared, three of which were tested as-built, and the other twelve samples were treated with different laser polishing conditions. For all the laser-polished tensile samples, the laser-polishing treatment was performed on their gage

sections. The starting point (blue point), the ending point (red point) and the laser polishing path were depicted in Fig. 1(c). Laser polishing was performed at a 50 W laser power with a 200 μm beam diameter and varied the velocity (100 mm/s and 200 mm/s) and the number of polishing pass (one and three passes). The overlap rate was 80 %, which corresponded to a step-over value between subsequent lines of 40 μm. For clarity, the different sets of laser polishing parameters are referred to as S1, S2, S3, and S4. The experiments were performed in a vacuum chamber at an absolute pressure of 0.07 Torr to help minimize surface oxidation and contamination. The detailed processing parameters for each of the four conditions are given in Table 2.

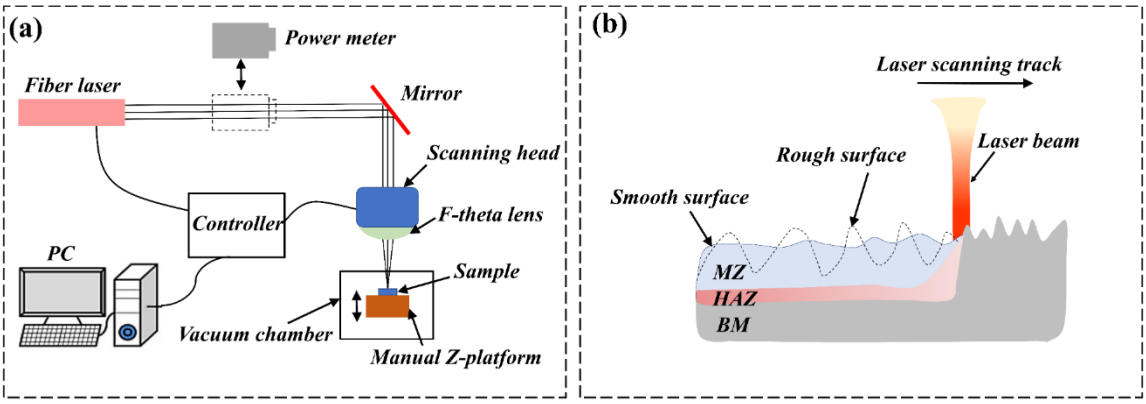

Fig. 2. (a) Schematic diagram of experimental setup for laser polishing; (b) schematic view of the remelting mechanism.

Table 2. Laser polishing parameters used in this study.

	S1	S2	S3	S4
Beam Diameter (μm)	200	200	200	200
Laser Power (W)	50	50	50	50
Line Spacing (mm)	0.04	0.04	0.04	0.04
Velocity (mm/s)	**100**	**200**	**100**	**200**
Number of Passes (-)	**1**	**1**	**3**	**3**

2.3. Microstructure observation and characterization

All samples were ultrasonically cleaned in acetone for 15 minutes, after which their surface morphologies were observed using an optical microscope (OM) (KEYENCE, VK-X250, Japan) and field emission scanning electron microscope (FE-SEM) (JEOL, JSM-7800F, Japan). The surface

roughness of all samples was measured by optical microscopy (OM) (KEYENCE, VK-X250, Japan) and subjected to a waviness filter of 250 μm. The surface roughness values reported represent the average of 10 different measurements. To observe the cross-sectional microstructure, the sample was cut perpendicular to the laser-polished surface. After mounting, grinding and polishing, samples were etched at room temperature using a solution (HCl: HNO_3: H_2O = 3:1:2) for approximately 50 s. The cross-sectional microstructure of the 316L were characterized by OM (KEYENCE, VK-X250, Japan) and FE-SEM (JEOL, JSM-7800F, Japan). The samples' surfaces were also analyzed by electron back-scattered diffraction (EBSD). The EBSD mapping was performed in an FE-SEM (JEOL, JSM-7800F, Japan) equipped with EBSD pattern acquisition software (TSL, OIM, USA) with a step size of 2 μm. In order to remove erroneous datapoints collected during EBSD, the data used to calculate grain diameter and misorientation angle was post-processed to remove grains with diameters less than 8 μm and misorientation angles smaller than 0.5 degrees.

Transmission electron microscope (TEM) (JEOL, JEM-2100, Japan) was used for deeper microstructural characterization. In order to obtain the microstructure close to the top surface layer, a protective layer was electroplated on the 316L top surface layer. Thin foils, approximately 1-mm-thick, parallel to the cross section, were cut by electro-spark wire-electrode cutting, and then manually ground to a thickness of approximately 100 μm. 3 mm diameter discs were punched from the foils. These discs were then electropolished by double jet electropolishing to produce standard samples conforming to TEM observation.

2.4. Cross-sectional microhardness measurement

The microhardness of the sub-surface of the samples was measured on their cross-section using a microhardness tester (Future-tech, FM-800, Japan) with a load of 25 g and a dwell time of 15 s. The average hardness value of each depth was measured from the polished surface to the bulk hardness level at intervals of 20 μm. The reported value was the average value of ten measurements.

2.5. Tensile property measurement

Tensile tests were carried out at room temperature by a tensile test machine (MTS, Sintech10/GL, USA) with a constant crosshead displacement rate of 1 mm/min. The strain was obtained by using an optical system incorporating a Digital Image Correlation System (DIC). Prior to the tensile test, the gage segments of each sample were sprayed with a random speckle pattern. During the test, the charge-coupled device camera was mounted in front of the sample and automatically acquired the image at 2 frames per second. After the test, the images were analyzed (Correlated Solutions, Vic-2D, USA) to calculate the strain evolution across the sample. Three samples were tested for each condition, and representative stress-strain curves were reported. The reported values were an average of three tests. Additionally, the fracture morphology of the tensile samples was examined via an FE-SEM (JEOL, JSM-7800F, Japan) to characterize the fracture behavior.

3. Results and discussion

3.1. Surface morphology

One of the limitations of the L-PBF process is the surface finish (i.e., roughness, waviness) that can be achieved. Fig. 3(a)-(e) show the 3D surface topographies of all samples. The as-built sample exhibits a periodic surface topography along the scanning direction of the L-PBF process (Fig. 3(a)). Many peaks and valleys are spotted on the top surface of the as-built sample, which has an average surface roughness Sa = 4.84 μm (Fig. 3(a)). The surface topography of all the post-processed (*i.e.*, laser-polished) samples shows a new orientation along the laser polishing direction indicated by the white arrow in Fig. 3(b)-(e). After polishing. the surface is smoothed with less peaks and valleys. It can be seen from the maximum and minimum on the scale bar (μm) that the peak-to-valley height of samples decreases from 118.53 μm to 52.02 μm, 69.80 μm, 36.08 μm, and 40.62 μm for S1, S2, S3, and S4, respectively. The maximum reduction of surface roughness (Sa) of S3 is approximately 86.6 % with a final Sa = 0.65 μm.

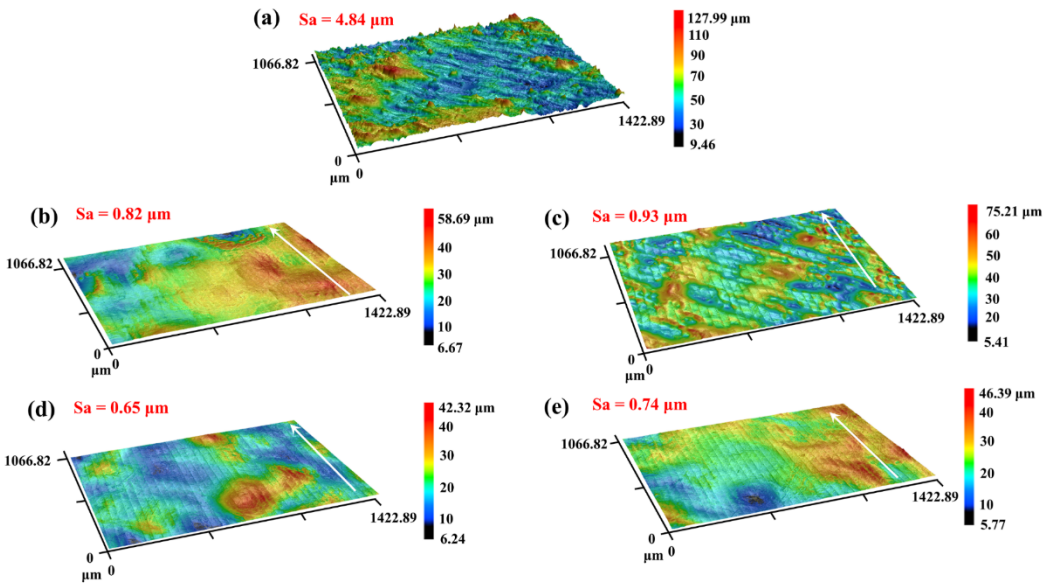

Fig. 3. Three-dimensional (3D) surface topographies of all samples: (a) as-built; (b) S1: 100 mm/s, one pass; (c) S2: 200 mm/s, one pass; (d) S3: 100 mm/s, three passes; (e) S4: 200 mm/s, three passes.

The top surface morphology under different conditions is shown at higher magnifications in Fig. 4. Many small powder particles and wave-like features at various scales exist on the as-built surface. The laser scanning tracks are continuous, forming clear ripples along the direction of the scanning track during the L-PBF process (Fig. 4(a)). Significant valleys can be seen between subsequent scanning tracks (Fig. 4(b)). Some powder particles remain on the surface (Fig. 4(b)), possibly due to incomplete melting of the powder or splashing of the particles. Those contribute to the relatively high surface roughness of the as-built 316L (Fig. 3(a)). After laser polishing, the surface is considerably smoother compared to the as-built samples. The powder particles, ripples, and valleys on the as-built 316L have disappeared or been significantly reduced in magnitude after laser polishing. The laser-remelted tracks are in the same direction as the laser polishing, as indicated by yellow arrow in Fig. 4(b). The laser-remelted tracks are not as clearly identifiable from Fig. 4(c). Residual bumps on the laser-polished surface are marked by ovals in Fig. 4(c), which may be due to the low energy density at a higher velocity (200 mm/s). After laser polishing at a velocity of 100 mm/s, a relatively flat surface with partially deposited material near the boundaries of individual laser-remelted tracks can be observed in Fig. 4(b). After three passes, the surface becomes smoother, especially for S3 (Fig. 4(d)), which agrees with the

previous observation that the surface roughness of the S3 is the lowest in Fig. 3(d).

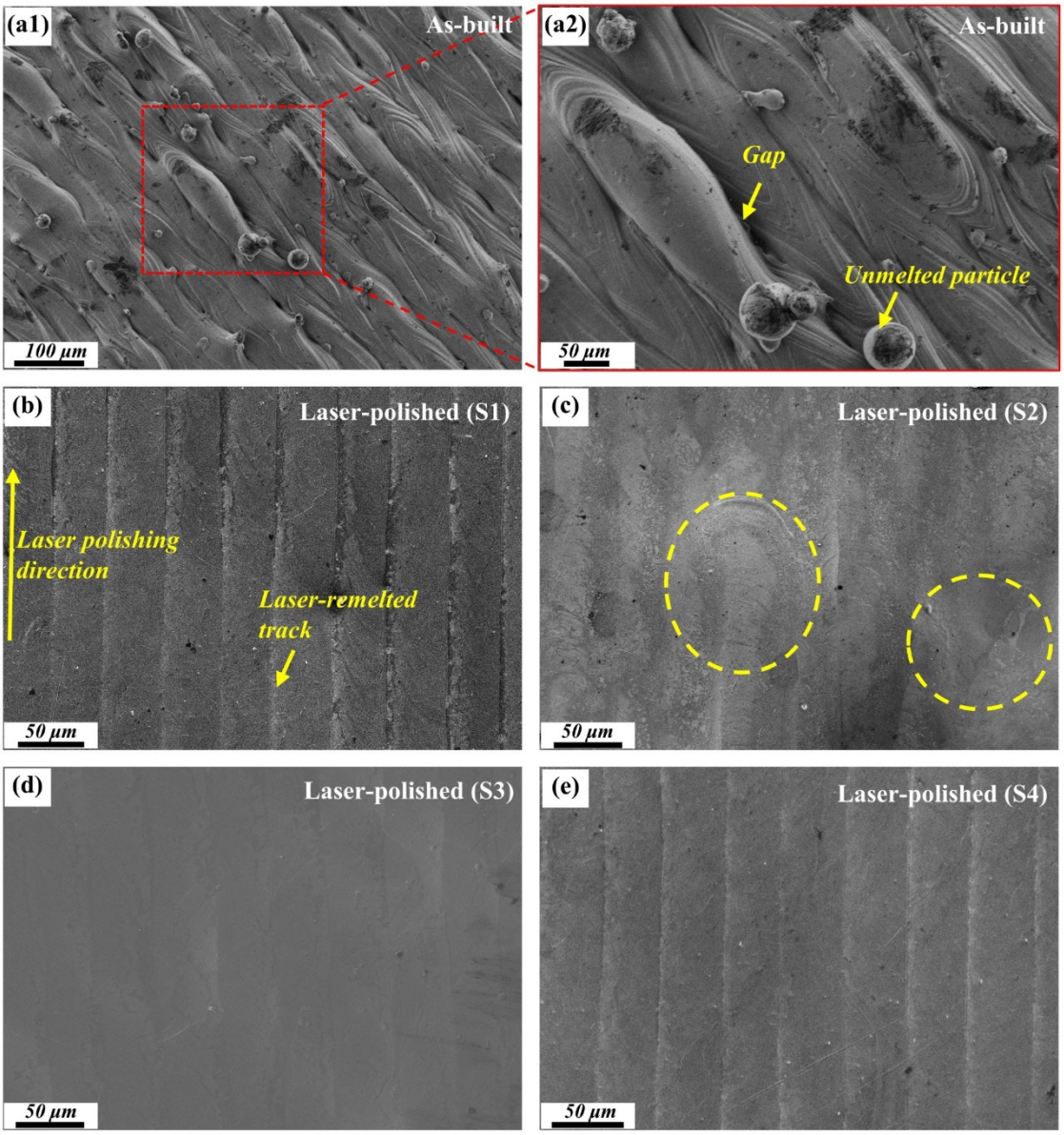

Fig. 4. SEM micrograph showing the top surface morphology of all samples: (a1) as-built; (a2) the magnified view of the rectangle in (a1); (b) S1: 100 mm/s, one pass; (c) S2: 200 mm/s, one pass; (d) S3: 100 mm/s, three passes; (e) S4: 200 mm/s, three passes.

Energy dispersive x-ray spectroscopy of the surface after laser polishing did not observe significant changes in the surface elemental composition except for higher nitrogen and oxygen quantities in the 200 mm/s samples compared to the 100 mm/s samples. However, it is not clear if the observed oxygen and nitrogen was from additional oxidation or leftover from initial concentrations on the as-printed

surface. To observe the grain morphology, size, orientation, and texture, EBSD mapping was performed on the top surface of the samples (Fig. 5). The black arrow in Fig. 5(b) is the direction of laser polishing. Since the crystal orientation in the Z (BD) direction is of interest, the inverse pole figure (IPF-Z plot) is presented to show grain morphology and orientation [25, 26]. It can be observed in Fig. 5(a) that the grains are arranged in a checkerboard-like pattern, which is related to the scanning strategy during L-PBF processing 316L (67° turning was used between layers) [27, 28]. The color-coded stereographic triangle inversed pole figure (IPF) is inserted in the bottom right corner of Fig. 5(b), where red, green, and blue represent the (001), (101), and (111) orientations, respectively. Most of the grains of the as-built sample show green (101) orientation in the IPF-Z plot image (Fig. 5(a)), which is attributed to the preferred growth direction of the grains. During the L-PBF process, a large temperature gradient is formed between the center and edge of the melt pool. The grains preferentially grow along the direction of the temperature gradient (*i.e.*, direction of heat flow) [29]. As shown in Fig. 5(b), after laser polishing, microstructural refinement appears to occur visually. However, the green (101) orientation remains the dominant direction on the IPF-Z. A <110> || BD fiber texture is also observed in both as-built and S3 samples (Fig. 5(c) and (d)). Bahl et al. [30] also found this fiber texture in 3D printed 316L stainless steel. Despite the overall fiber characteristic of the texture, the texture index for the as-built and S3 sample is 4.51 and 5.49, respectively. By remelting the surface during laser polishing, new epitaxial grain growth occurs from the previous grains. This may be the reason for the texture strengthening following polishing.

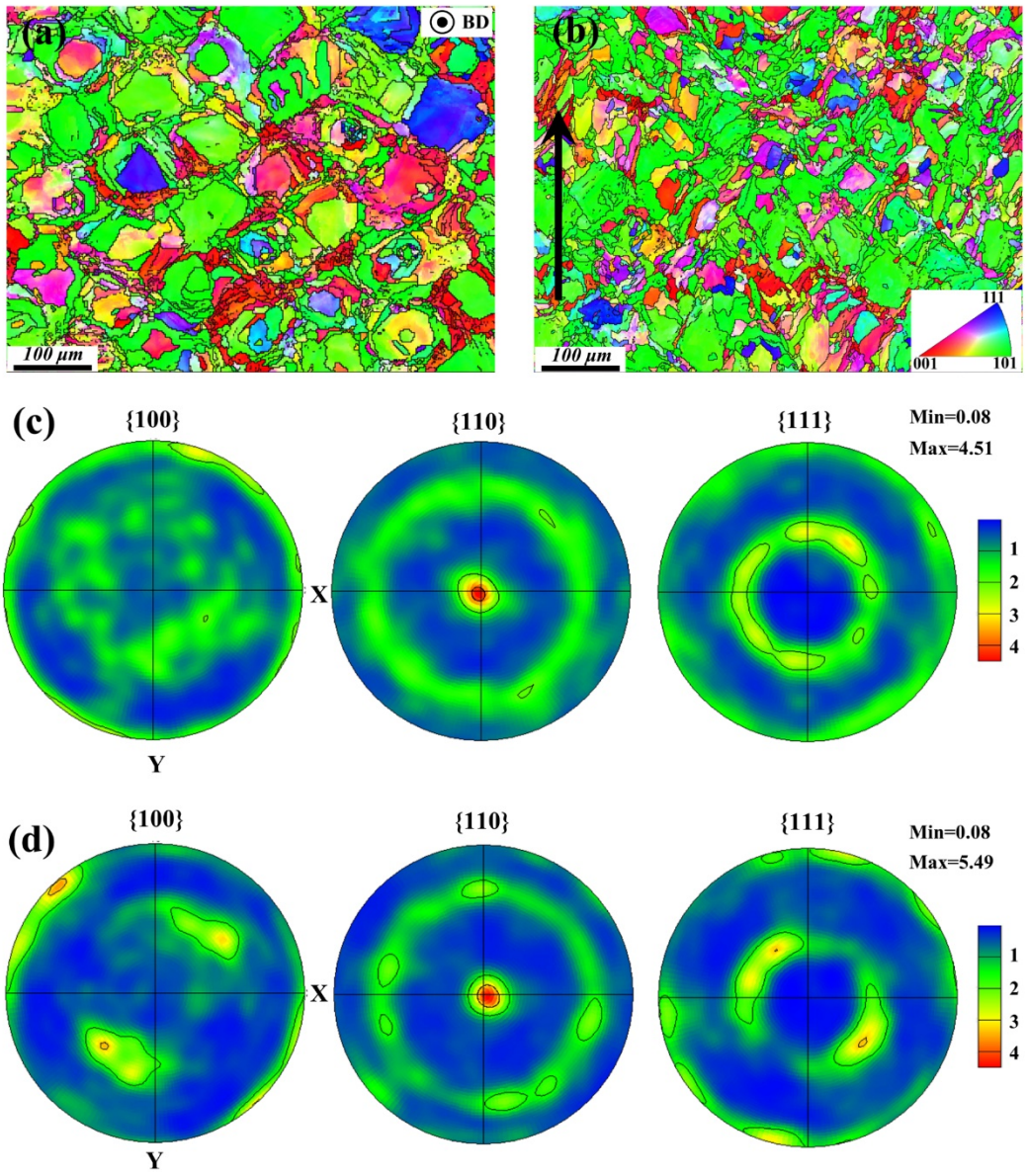

Fig. 5. EBSD orientation maps from the top view of (a) the as-built sample and (b) laser-polished sample (S3); corresponding pole figures for (c) the as-built sample and (d) laser-polished sample (S3).

In order to more clearly show the effect of laser polishing on the surface grain morphology, the laser-polished surface is observed at a higher magnification. As shown in Fig. 6, after laser polishing, the grain is found to be partially orientated along the direction of laser polishing (marked by the black arrow). This demonstrates that the laser polishing path influences the grain morphology and elongation direction.

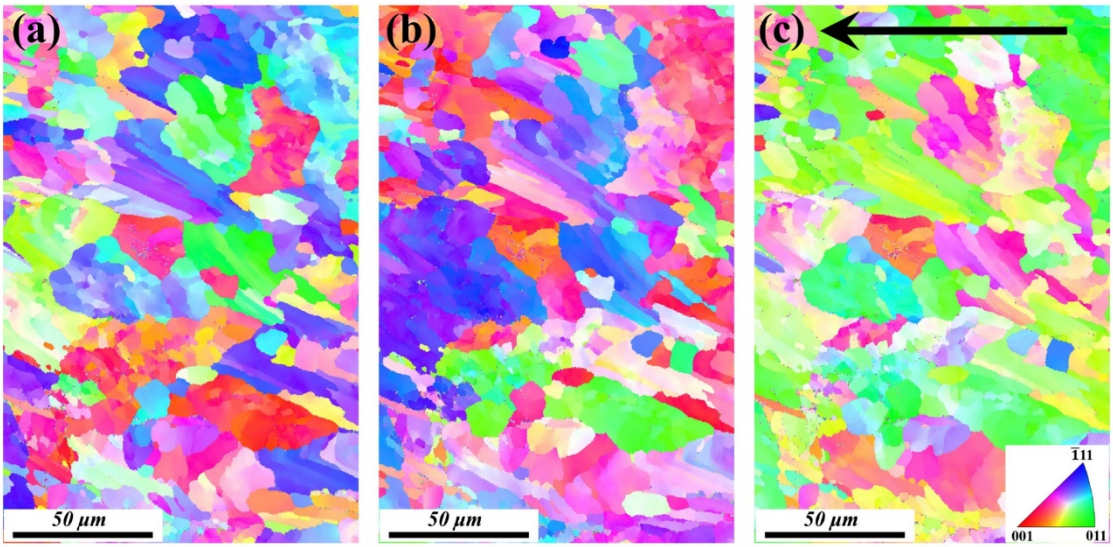

Fig. 6. EBSD orientation maps from the top view of laser-polished sample (S3): (a) IPF-X; (b) IPF-Y; and (c) IPF-Z.

In this analysis, grains with size less than 8 μm and misorientation angle of less than 0.5 degrees were defined as erroneous datapoints and removed. In order to quantitatively analyze the effect of laser polishing on the average grain size, Fig. 7(a) and (b) depicts the histogram of grain size of the as-built and S3 sample, respectively. For the as-built sample, the fraction of grains with size smaller than 10 μm accounts for 16.4 %, and the average grain diameter is approximately 18.4 μm (Fig. 7(a)). It can be seen that the S3 sample shows a refined microstructure (Fig. 5(b)). The average grain diameter of the S3 sample is 17.3 μm, and grains (diameter < 10 μm) occupy 23.2% (Fig. 7(b)). The distribution of grain boundary misorientation of the as-built and S3 sample is obtained by EBSD, as presented in Fig. 7(c) and (d), respectively. For both the as-built and S3 sample, most of the grain boundaries are found to be low angle grain boundaries (LAGBs) (2°<LAGBs<15°). In particular, the grain boundaries between 2°~5° account for 53.4% in the as-built samples (Fig. 7(c)), while it is increased to 64.6% after laser polishing (Fig. 7(d)). It is well known that the LAGB located between 2°~5° is not a true grain boundary, but a sub-grain boundary formed by rearrangement of dislocations. [29, 31]. The aspect ratio distribution of the two samples are shown in Fig. 7(e) and (f). After laser polishing, the average aspect ratio is slightly increased.

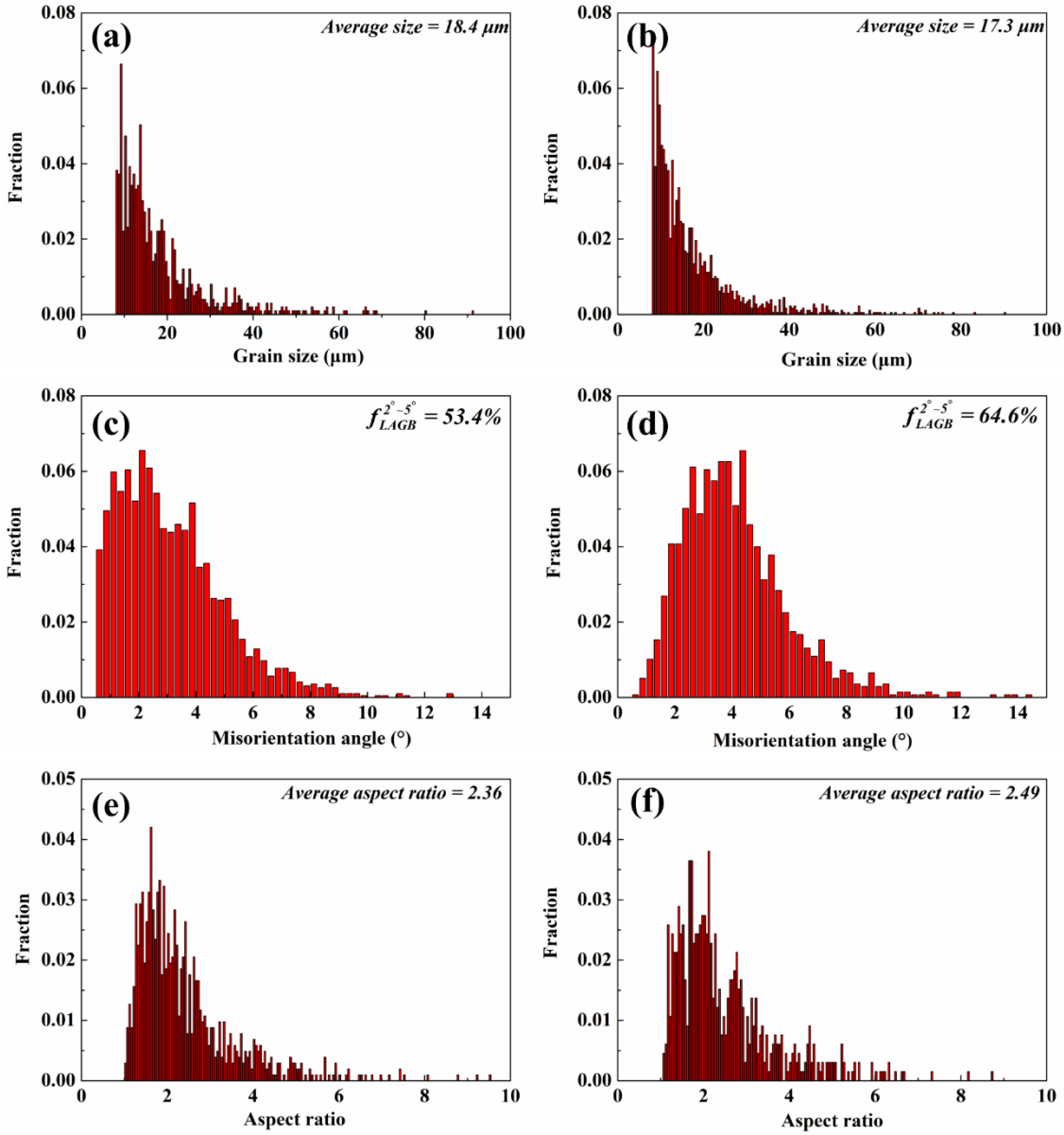

Fig. 7. EBSD grain size distribution of (a) as-built sample and (b) laser-polished sample (S3); and grain boundary misorientation distribution of (c) as-built sample and (d) laser-polished sample (S3); grain aspect ratio distribution of (e) as-built sample and (f) laser-polished sample (S3).

3.2. Microstructure analysis

Fig. 8(a1) and (a2) show the microscopic properties of the as-built sample in the cross section, where the building direction (BD) of L-PBF is marked by a red arrow in Fig. 8(a1). The top surface of the as-built sample is uneven because of the poor surface quality previously reported in §3.1 (Fig. 4(a1)).

Because L-PBF processing is a characteristic of layer-by-layer processing, it can be easily seen that the layers of the melt pool are stacked on the cross section. The average depth of the melt pool is more than 50 μm and the width of melt pool is observed to be greater than 100 μm (Fig. 8(a2)).

The cross-section of the laser-polished sample is also analyzed to confirm the subsurface microscopic properties, as shown in Fig. 8(b)-(d). Compared with Fig. 8(a2), the top surface of the sample is much flatter. The size of the melt pool left by laser polishing is considerably smaller than that produced by L-PBF, with a larger aspect ratio between the width and depth of the melt pool. Moreover, the melt pool has an average depth of approximately 28.1 μm for the S1 (100 mm/s velocity) condition verses an average depth of 21.7 μm for the S2 (200 mm/s velocity) condition. As the number of polishing passes increases to three, the average depth of the melt pool increases to 42.7 μm (S3, 100 mm/s velocity) and 35.9 μm (S4, 200 mm/s velocity), which represents an increase of 52 % and 65 %, respectively, over the single pass tests. As the laser velocity increases, the depth of melt pool is reduced.

In continuous wave polishing, the energy density E (J/mm^2) of the laser can be defined by Eq. (1) [32]:

$$E = \frac{P}{DV_f} \tag{1}$$

where P is the laser power (W), D is beam diameter (mm), and V_f is velocity (mm/s). Chang et al. [33] also reported that within a certain range, the depth of the melt pool increases as the laser energy density increases. Since the laser velocity is inversely proportional to laser energy density, when the laser velocity is 100 mm/s, a deeper melt pool would be expected. When the velocity decreases from 200 mm/s to 100 mm/s, the average depth of the melt pool increases by 29 % (one pass) and 19 % (three passes). Both the number of polishing pass and the velocity have an effect on the average depth of the melt pool, and the influence of the former is greater. Interestingly, the depth of the deepest melt pool of the three pass samples (Fig. 8(d) and (e)) seems to be deeper than the deepest melt pool of the single pass samples Fig. 8(b) and (c). The deepest melt pool visible in the three pass samples appears to be from the second of the three passes. While the cause for the variation in the melt pool depth is not known, it may be that the first laser pass left an oxide film (Fig. 4(b) and (c)) on the surface that increased the laser absorption in the second pass causing a deeper melt pool. Approximately 5 minutes was waited

between each pass on the multi-pass samples to ensure an equalized temperature field across the sample. However, it is possible that the material started at an elevated temperature for the later passes, which could also contribute to the variance in the melt pool depth.

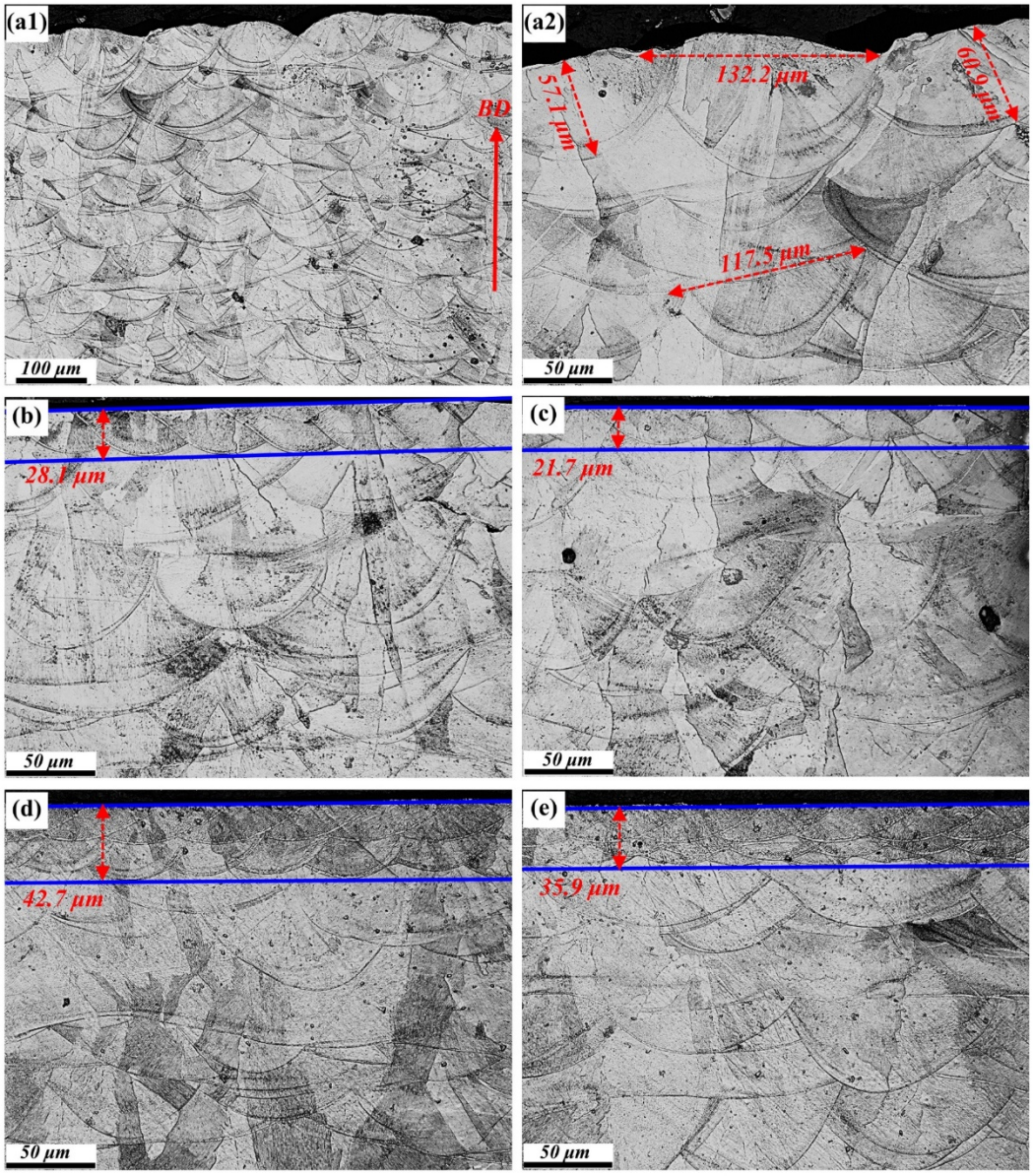

Fig. 8. Optical micrograph of cross section of all samples: (a1) as-built at a low magnification; (a2) as-built at a high magnification; (b) S1: 100 mm/s, one pass; (c) S2: 200 mm/s, one pass; (d) S3: 100 mm/s, three passes; (e) S4: 200 mm/s, three passes.

Fig. 9 shows the as-built microstructure in a cross-section perpendicular to the final L-PBF building layer and parallel to the building direction (BD) marked by the white arrow in Fig. 9(a). Long columnar

grains are observed in the build direction. This phenomena has been frequently reported for L-PBF processed parts [34, 35]. Their formation is due to the temperature gradient during processing, the preferred <001> growth direction of the austinite during solidification, and epitaxial grain growth from the grains of the previous layer [29, 36]. Within the columnar grains both columnar and cellular sub-grain structures can be observed that are believed to be primary dendrites without secondary arms due to their preferred growth direction (Fig. 9(b), (c), and (d)). As indicated by the yellow arrows in Fig. 9(a), the columnar structures tend to grow perpendicular to the melt pool boundary (Fig. 9(c) and (d)), which is the direction of the heat flow. However, these columnar structures may be a remnant of the sample sectioning and may actually be the cellular structure sectioned at an angle. At the overlapping region between two melt pools, cellular structures can be seen (Fig. 9(b)). As seen in Fig. 10(a) and (b), after laser polishing, the cellular structures in the S3 sample appear to be more common than the as-built sample. In addition, the bottom of the melt pool formed after laser polishing also has a columnar structure (Fig. 10(c)). The size of the cellular structure changes somewhat along the depth direction, and there is a thin layer of cells at the top surface layer that are smaller and cover the entire surface (Fig. 10(d)).

Further microstructure analysis was conducted using TEM characterization. The microstructures, including dislocations and dislocation cells, can be seen in TEM images obtained from the as-built samples (Fig. 9(e) and (f)). The initial columnar structures consist of a large number of dislocation structures (Fig. 9(e)). Fig. 9(f) shows that many dislocations are arranged within the interdendritic region. The average diameter of the dislocation cells is approximately 0.6 μm, which corresponds to the cellular structures observed in the etched samples (Fig. 9(b)). Additional dislocations can also be observed within the dislocation cells. After laser polishing, the dislocation density within the cellular structures appears to qualitatively increase, and many dislocations appear to gather in the interdendritic region to form larger dislocation walls (Fig. 10(e) and (f)). Dislocation tangles can also be observed in the interdendritic region (Fig. 10(e) and (f)).

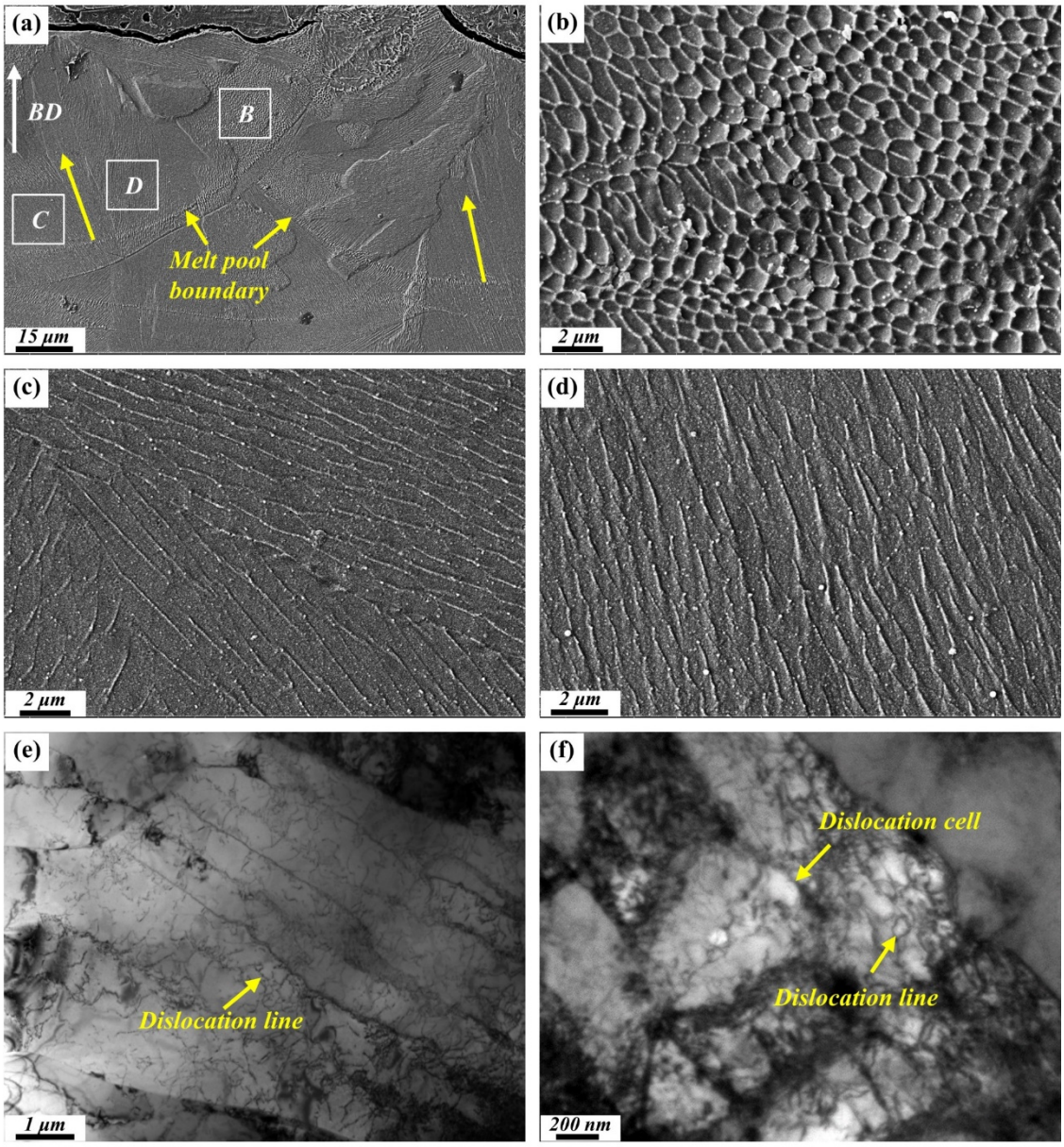

Fig. 9. SEM images showing characteristic cross-sectional microstructure of as-built sample: (a) the SEM image at low magnification; (b)-(d) the enlarged view of B, C, and D in (a) respectively; (e) and (f) TEM images.

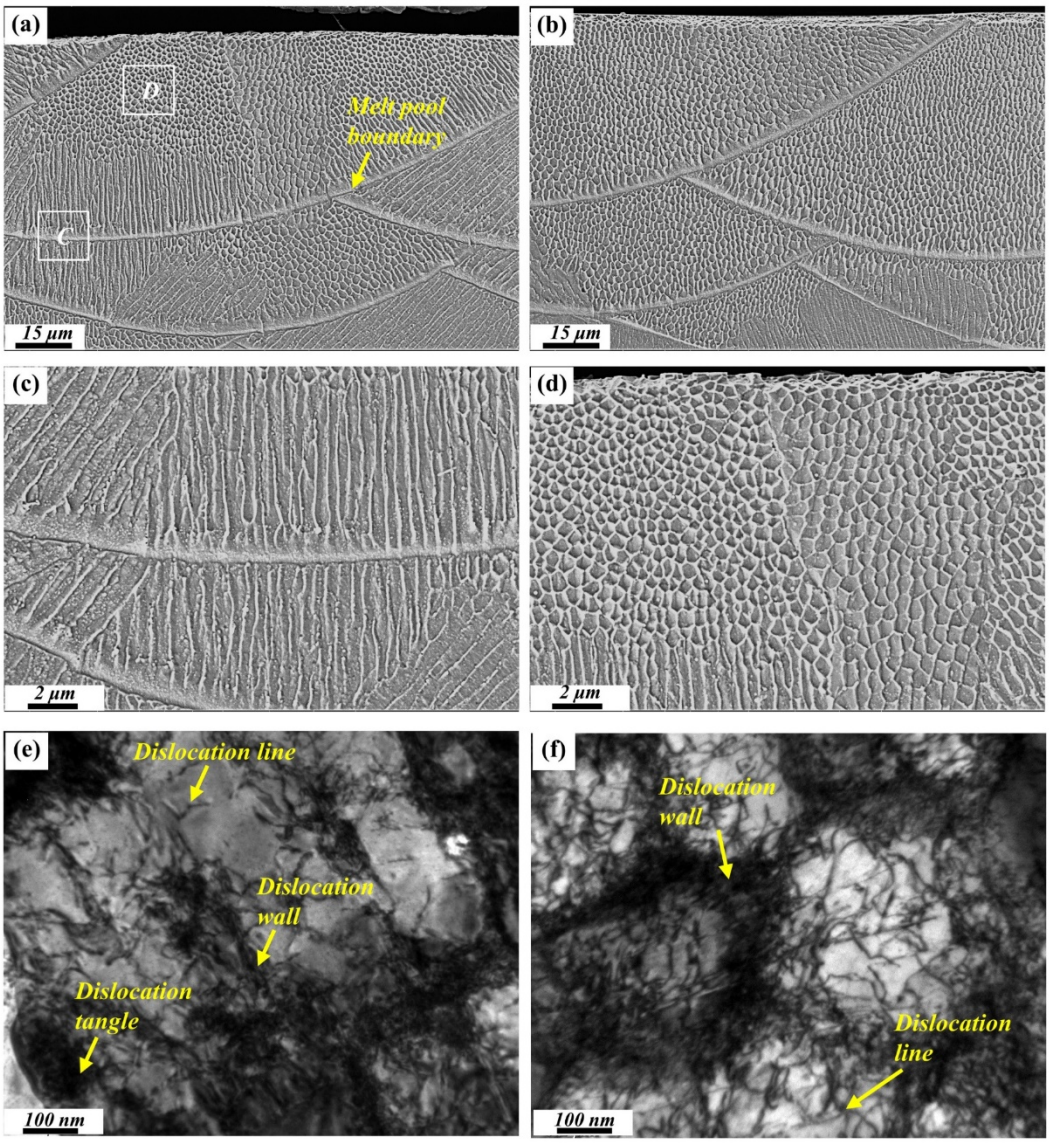

Fig. 10. SEM images showing characteristic cross-sectional microstructure of S3 sample: (a) and (b) the SEM image at low magnification; (c)-(d) the enlarged view of C and D in (a) respectively; (e) and (f) TEM images.

3.3. Cross-sectional microhardness measurement

To assess the depth of the affected layer, all samples were subjected to in-depth microhardness measurements. As illustrated in Fig. 11(a), the mean microhardness of as-built sample is approximately 208 HV and remains relatively constant with depth. After laser polishing, the maximum hardness (~10 μm from the top surface) of S1, S2, S3 and S4 reaches 241 HV, 228 HV, 262 HV and 256 HV, respectively. Additionally, a hardened layer is formed in the material after laser polishing. Bhaduri et al. [16] and Fang et al. [37] also

reported a gradient hardened layer induced by laser polishing of AM parts. Fig. 11(a) shows that the thickness of the hardened layer is between 50 μm and 70 μm, beyond which all the samples have the same hardness as the base material. It is worth noting that the thickness of the hardened layer is larger than that of the melt pool formed by laser polishing shown in Fig. 8. It has been reported in other literature [24] that laser polishing not only forms a certain depth of melting zone (MZ) in the sample (i.e., the formed melt pool in Fig. 8), but also forms a heat affected zone (HAZ). Yung et al. [38] and Lamikiz et al. [39] also reported an increase in hardness at the HAZ, although the HAZ and the base material (BM) cannot be clearly distinguished in Fig. 8. Fig. 11(a) also demonstrates that multiple passes cause a further increase in hardness and depth of the HAZ layer. This indicates thermal cycling influences the hardness and depth of the affected layer. Other work examining spot welding has shown that the hardness of the HAZ layer is higher than that of the BM layer due to the thermal stress cycling [40, 41]. As show in Fig. 11(b), the average sub-surface hardness (~10 μm from the top surface) of the samples polished by only one pass is 235 HV, while it is increased to 259 HV after three passes, which is an increase of 10.2%. The laser velocity also influences the sub-surface hardness, but to a smaller degree than number of passes. When the laser velocity decreases from 200 mm/s to 100 mm/s, the average hardness of the sub-surface is increased to 252 HV, which is only an increase of 3.7% (Fig. 11(c)).

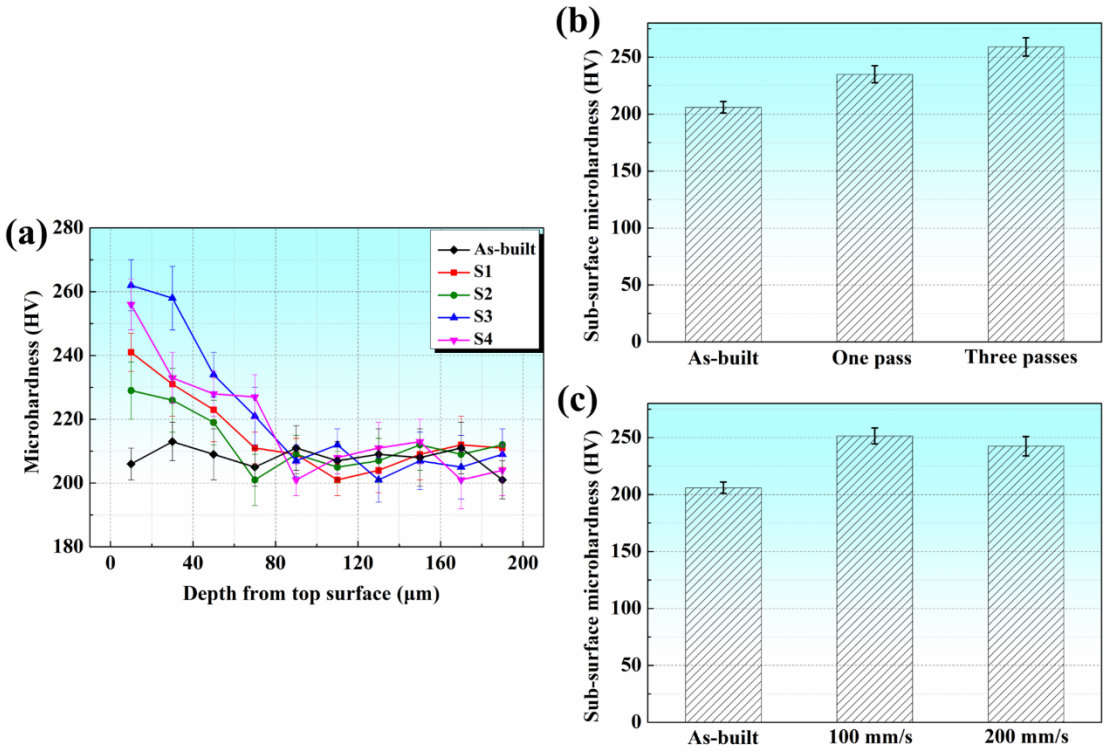

Fig. 11. (a) Microhardness profile on cross-section with different laser polishing treatments; (b) the average sub-surface micro-hardness for different number of scanning pass (label 'One pass' represents the average value of S1 and S2, label 'Three passes' represents the average value of S3 and S4); (c) the average sub-surface micro-hardness of different scanning velocity (label '100 mm/s' represents the average value of S1 and S3, label '200 mm/s' represents the average value of S2 and S4).

3.4. Tensile test

3.4.1. Tensile properties

Fig. 12(a) presents representative engineering stress-strain curves of samples at different conditions. All engineering stress-strain curves of as-built and the S3 samples are also included in Fig. 12(b). The results of tensile tests are summarized in Fig. 13. Since it is difficult to determine the point of ultimate tensile strength from the plots, the stress at a specified strain of 20% ($\sigma_{20\%}$) is used to evaluate the effect of laser polishing on tensile properties. It is observed that the stress at a specified strain of 20% ($\sigma_{20\%}$) after laser polishing is increased. The stress of the as-built sample is 621 ± 10 MPa and the maximum increase in stress is approximately 7.7 % with a final value of 669 ± 7.5 MPa (S3) (Fig. 13(a)). As the number of passes increases from one to three, the average stress increases from 642 ± 10 MPa to 666 ±

8.5 MPa with an increase of 3.8 % (Fig. 13(b)). However, the average stress ($\sigma_{20\%}$) only increases by 1.0 % when the velocity decreases from 200 mm/s to 100 mm/s (Fig. 13(c)), indicating that the velocity of laser polishing has a smaller effect on the tensile strength than number of passes. It can be seen from Fig. 8 that the effect of the number of pass on the increase of the average depth of melt pool is higher than that caused by the change in the velocity. The mean elongation-at-break (EL) values of the as-built, S1, S2, S3, and S4 conditions are 58.3 ± 1.6 %, 59.7 ± 0.6 %, 59.1 ± 0.6 %, 63.3 ± 0.3 % and 62.3 ± 0.5 %, respectively (Fig. 13(a)). This represents an increase in EL of the S3 condition compared to the as-built sample of 8.6 %. Therefore, the laser polishing treatment also increases the EL of stainless steel 316L. It can also be found in Fig. 13(b) and (c) that the effect of the number of passes on the EL is greater than the velocity. There is usually an inverse correlation between strength and ductility. However, in this study, it is worth noting that all post-processed samples exhibit increased stress and ductility. Additionally, while only the top surface of the tensile samples was laser-polished, further improvements in the tensile properties may be observed by polishing the other three sides.

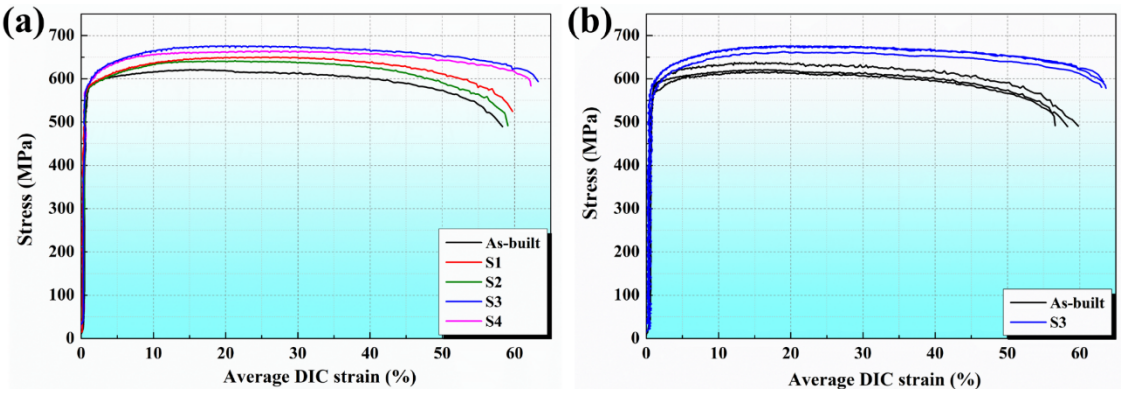

Fig. 12. (a) Representative engineering stress-strain curves of all samples from DIC data; (b) all engineering stress-strain curves of as-built and the laser-polished (S3) samples.

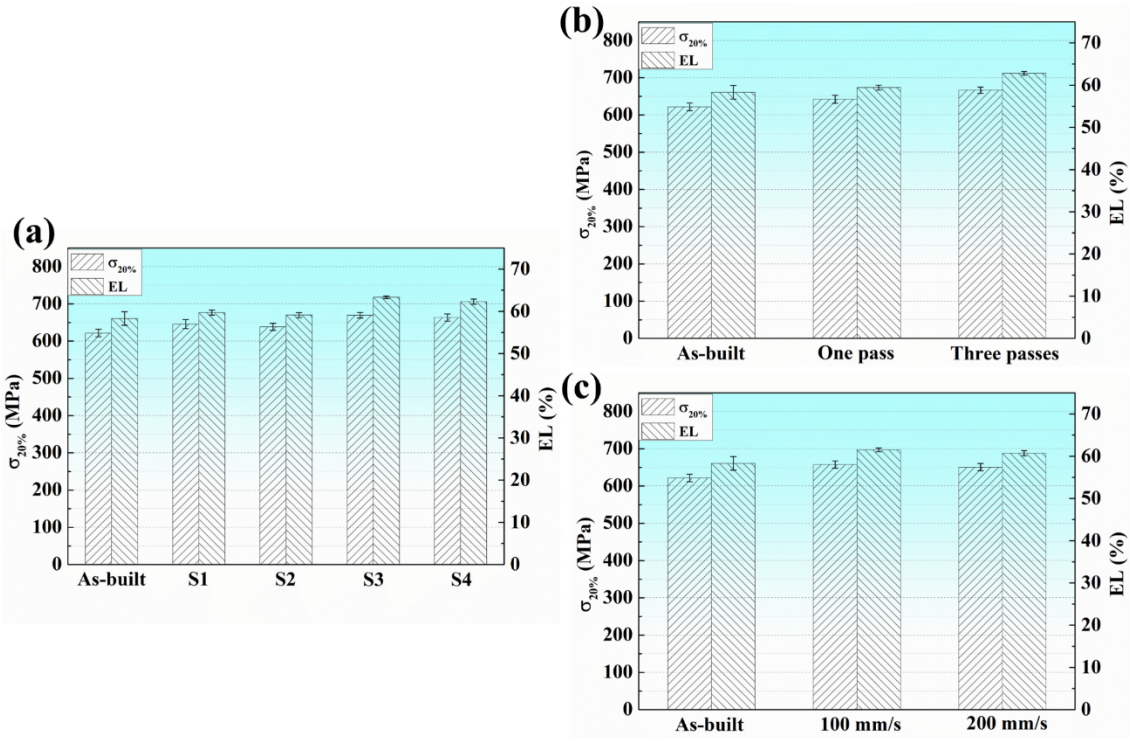

Fig. 13. Stress at a specified strain of 20% ($\sigma_{20\%}$) and elongation-at-break (EL) of all samples; (b) the average stress a specified strain of 20% ($\sigma_{20\%}$) and elongation-at-break (EL) for different number of pass; (c) the average stress a specified strain of 20% ($\sigma_{20\%}$) and elongation-at-break (EL) of different velocity.

3.4.2. The fracture morphology

The fracture surfaces near the top surface of the as-built and S3 samples were also observed using SEM to study the fracture behavior of the tensile tests. The white arrows in Fig. 14 refer to the building direction (BD). Fig. 14(a1) shows the fracture surface of the as-built sample. At a higher magnification (Fig. 14(a2)), it can be seen that a large number of dimples with various sizes are distributed on the fracture surface, which indicates that ductile fracture is a primary fracture mechanism. The fracture surface morphology of the laser-polished sample is shown in Fig. 14(b1). Although a large number of dimples are also observed on the fracture surface after laser polishing (Fig. 14(b2)), the dimples appear to be larger and deeper than those in the as-built sample, which implies a more ductile fracture [42-44]. Generally, the size of the dimple is positively correlated with the material plasticity [45]. According to the report of Irizalp et al. [46], large and deep dimples indicate a more ductile rupture mode. Similar conclusions can be found in many other sources [42, 43, 47]. This also agrees with the tensile test results,

which observed a higher elongation-at-break.

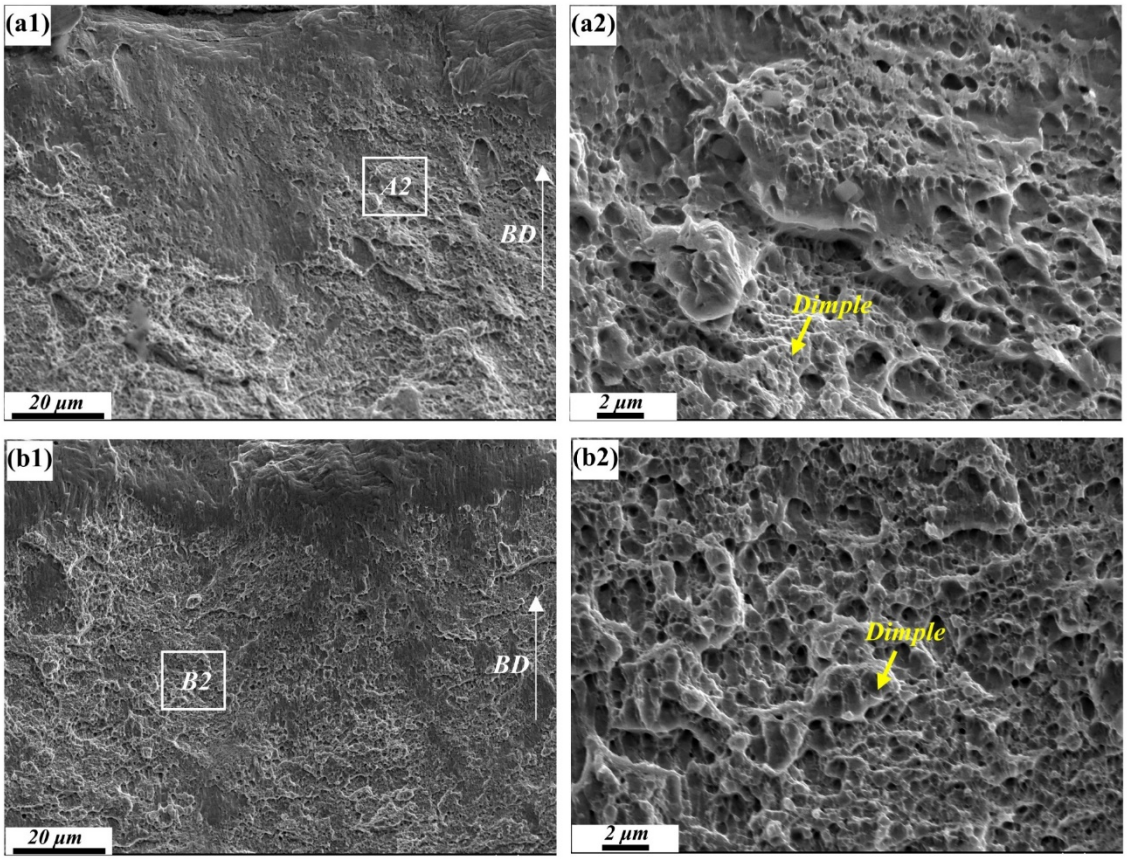

Fig. 14. Typical SEM images of the fracture surface from (a1) a failed as-built sample; (b1) a laser-polished sample; (a2) and (b2) the enlarged view of A2 and B2 in (a1) and (b1), respectively.

Generally, the ductility of a metal material decreases as the strength increases [48]. In contrast, both strength and ductility were seen to increase in this experiment after polishing. Laser polishing of L-PBF samples may be beneficial in three ways. Firstly, some surface defects in the L-PBF process, such as incompletely melted particles, balled particle agglomerates, and gaps will be the source of stress concentrations during tensile testing and influence the fracture behavior of 316L. After laser polishing, the frequency of those surface defects significantly decreases (Fig. 4), which contribute to the improvement of tensile strength and ductility. Secondly, a refined structure is formed in the near surface region of the sample after laser polishing (Fig. 10(d)). Grain refinement is one strengthening method that can increase the strength while also improving the plasticity of the material to a certain extent. This has been used to obtain high strength and high ductility materials [46, 49] and may be contributing to

the higher strength and ductility observed in this work. Finally, the amount of high-density dislocation structures such as dislocation tangles and dislocation walls appear to increase following laser polishing (Fig. 10). These interactions of entangled dislocation will restrain the movement of dislocations to contribute to the increased strength. According to the dislocation structure model of LAGBs [50-52], the contribution of the LAGBs to material strengthening can be related to the contribution of dislocation density. After laser polishing, the proportion of the LAGBs (2°~5°) increases (Fig. 7(d)), indicating an introduction of additional dislocations that could increases the dislocation enhancement effect.

4. Conclusions

In this work, the microstructure and mechanical properties of L-PBF 316L samples post-processed using laser polishing (via remelting) have been studied. The main conclusions are as follows:

(1) A maximum reduction in the surface roughness *Sa* of up to 86.6% (from 4.84 μm to 0.65 μm) was accomplished by using 100 mm/s laser velocity and three passes with surfaces typically exhibiting with no signs of powder particles, ripples, and gaps as compared to the as-built samples.

(2) Laser polishing refined the grains of the remelted region of L-PBF 316L and the areal fraction of grains with sizes smaller than 10 μm increased from 16.4 % to 23.2 %. The aspect ratio of the grains slightly increased from 2.36 to 2.49 after laser polishing. The average grain size of the laser-polished sample was 17.3 μm, which was refined compared with that of the as-built sample. The amount of LAGBs (2°~5°) increased from 53.4 % to 64.6 %, indicating that the density of dislocations was increased. Compared with the as-built part, the proportion of cellular sub-structures has increased significantly after laser polishing. The dislocation wall and dislocation tangles occurred at the sub-structure boundaries and within some sub-structures, and appeared to be more pronounced following polishing.

(3) The number of passes and the velocity of laser polishing had a large effect on the micro-hardness. Three passes of polishing with a velocity of 100 mm/s gave the highest micro-hardness of all the conditions. In addition, laser polishing created a hardened layer which penetrated approximately ~50-70 μm into the surface of the 316L. Decreasing velocity and increasing the number of pass both

increased the depth of the hardened layer.

(4) Compared to the as-built samples, both the tensile strength and ductility of 316L were increased after laser polishing. Larger and deeper dimples were observed on the polished fracture surface, which indicated a more ductile fracture. This enhancement could be attributed to grain refinement, the elimination of defects, and the dislocation strengthening after laser polishing.

These conclusions demonstrate that laser polishing can reduce the surface roughness of as-built L-PBF parts while also introducing beneficial changes to tensile properties. The reduced surface roughness that can be produced by laser polishing is expected to have a greater influence on the wear behavior, friction, corrosion resistance, and fatigue crack initiation of L-PBF parts. Therefore, ongoing research is looking into the effect of laser polishing on these surface properties in order to better understand how laser polishing can be used for post-processing additive manufactured parts.

Acknowledgments

This work was supported by the National Natural Science Foundation of China grant No. 51975261, the U.S. National Science Foundation grant CMMI-1727366, LasX Industries, Inc., NSF-supported shared facilities at the University of Wisconsin-Madison. the Grainger Institute for Engineering, and the UW2020 program at the University of Wisconsin–Madison.

References

[1] E.O. Olakanmi, R.F. Cochrane, K.W. Dalgarno, A review on selective laser sintering/melting (SLS/SLM) of aluminium alloy powders: Processing, microstructure, and properties, Prog. Mater. Sci. 74 (2015) 401-477.
[2] J.P. Kruth, L. Froyen, J. Van Vaerenbergh, P. Mercelis, M. Rombouts, B. Lauwers, Selective laser melting of iron-based powder, J. Mater. Process. Technol. 149(1-3) (2004) 616-622.
[3] J.F. Sun, Y.Q. Yang, D. Wang, Parametric optimization of selective laser melting for forming Ti6Al4V samples by Taguchi method, Opt. Laser Technol. 49 (2013) 118-124.
[4] B. Zhou, J. Zhou, H.X. Li, F. Lin, A study of the microstructures and mechanical properties of Ti6A14V fabricated by SLM under vacuum, Mater. Sci. Eng. A 724 (2018) 1-10.
[5] M.T. Mohammed, Mechanical Properties of SLM-Titanium materials for biomedical applications: a review, Mater. Today Proc. 5(9) (2018) 17906-17913.
[6] C.Y. Yap, C.K. Chua, Z.L. Dong, Z.H. Liu, D.Q. Zhang, L.E. Loh, S.L. Sing, Review of selective

laser melting: Materials and applications, Appl. Phys. Rev. 2(4) (2015) 041101.
[7] C. Tian, X. Li, H. Li, G. Guo, L. Wang, Y. Rong, The effect of porosity on the mechanical property of metal-bonded diamond grinding wheel fabricated by selective laser melting (SLM), Mater. Sci. Eng. A. 743 (2019) 697-706.
[8] C. Galy, E. Le Guen, E. Lacoste, C. Arvieu, Main defects observed in aluminum alloy parts produced by SLM: From causes to consequences, Addit. Manuf. 22 (2018) 165-175.
[9] Y.M. Wang, T. Voisin, J.T. McKeown, J. Ye, N.P. Calta, Z. Li, Z. Zeng, Y. Zhang, W. Chen, T.T. Roehling, R.T. Ott, M.K. Santala, P.J. Depond, M.J. Matthews, A.V. Hamza, T. Zhu, Additively manufactured hierarchical stainless steels with high strength and ductility, Nature Materials 17(1) (2018) 63-71.
[10] E. Ukar, A. Lamikiz, L.N.L. de Lacalle, F. Liebana, J.M. Etayo, D. del Pozo, Laser polishing operation for die and moulds finishing, Adv. Mater. Res. 83-86 (2009) 818-825.
[11] A.M.K. Hafiz, E.V. Bordatchev, R.O. Tutunea-Fatan, Influence of overlap between the laser beam tracks on surface quality in laser polishing of AISI H13 tool steel, J. Manuf. Process. 14(4) (2012) 425-434.
[12] T.L. Perry, D. Werschmoeller, X. Li, F.E. Pfefferkorn, N.A. Duffie, The effect of laser pulse duration and feed rate on pulsed laser polishing of microfabricated nickel samples, J. Manuf. Sci. Eng. 131(3) (2009) 031002.
[13] G. Telasang, J.D. Majumdar, G. Padmanabham, I. Manna, Structure–property correlation in laser surface treated AISI H13 tool steel for improved mechanical properties, Mater. Sci. Eng. A. 599 (2014) 255-267.
[14] T.L. Perry, D. Werschmoeller, X. Li, F.E. Pfefferkorn, N.A. Duffie, Pulsed laser polishing of micro-milled Ti6Al4V samples, J. Manuf. Process. 11(2) (2009) 74-81.
[15] J. Kumstel, B. Kirsch, Polishing titanium-and nickel-based alloys using cw-laser radiation, Phys. Procedia 41 (2013) 362-371.
[16] D. Bhaduri, P. Penchev, A. Batal, S. Dimov, S.L. Soo, S. Sten, U. Harrysson, Z. Zhang, H. Dong, Laser polishing of 3D printed mesoscale components, Appl. Surf. Sci. 405 (2017) 29-46.
[17] B. Rosa, P. Mognol, J.-Y. Hascoët, Laser polishing of additive laser manufacturing surfaces, J. Laser Appl. 27(S2) (2015) S29102.
[18] E. Yasa, J.-P. Kruth, Application of laser re-melting on selective laser melting parts, Adv. Prod. Eng. Manag. 6(4) (2011) 259-270.
[19] P. Nieslony, G. Krolczyk, S. Wojciechowski, R. Chudy, K. Zak, R. Maruda, Surface quality and topographic inspection of variable compliance part after precise turning, Appl. Surf. Sci. 434 (2018) 91-101.
[20] L. Chen, B. Richter, X. Zhang, X. Ren, F.E. Pfefferkorn, Modification of surface characteristics and electrochemical corrosion behavior of laser powder bed fused stainless-steel 316L after laser polishing, Addit. Manuf. (2020) 101013.
[21] K. Kumar, A. Pooleery, K. Madhusoodanan, R. Singh, J. Chakravartty, B. Dutta, R. Sinha, Use of miniature tensile specimen for measurement of mechanical properties, Procedia Eng. 86 (2014) 899-909.
[22] J.S. Hoppius, L.M. Kukreja, M. Knyazeva, F. Pöhl, F. Walther, A. Ostendorf, E.L. Gurevich, On

femtosecond laser shock peening of stainless steel AISI 316, Appl. Surf. Sci. 435 (2018) 1120-1124.
[23] E.V. Bordatchev, A.M. Hafiz, O.R. Tutunea-Fatan, Performance of laser polishing in finishing of metallic surfaces, Int. J. Adv. Manuf. Technol. 73(1-4) (2014) 35-52.
[24] A. Lamikiz, J. Sanchez, L.L. De Lacalle, D. Del Pozo, J. Etayo, J. Lopez, Laser polishing techniques for roughness improvement on metallic surfaces, Int. J. Nanomanuf. 1(4) (2007) 490-498.
[25] P. Wang, B. Zhang, C.C. Tan, S. Raghavan, Y.-F. Lim, C.-N. Sun, J. Wei, D. Chi, Microstructural characteristics and mechanical properties of carbon nanotube reinforced Inconel 625 parts fabricated by selective laser melting, Mater. Des. 112 (2016) 290-299.
[26] D. Deng, R.L. Peng, H. Brodin, J. Moverare, Microstructure and mechanical properties of Inconel 718 produced by selective laser melting: Sample orientation dependence and effects of post heat treatments, Mater. Sci. Eng. A. 713 (2018) 294-306.
[27] M.S. Pham, P. Hooper, Roles of microstructures on deformation response of 316 stainless steel made by 3D printing, American Institute of Physics Conference Series, 2017.
[28] M.S. Pham, B. Dovgyy, P.A. Hooper, Twinning induced plasticity in austenitic stainless steel 316 L made by additive manufacturing, Mater. Sci. Eng. A. 704 (2017) 102-111.
[29] A. Kreitcberg, V. Brailovski, S. Turenne, Effect of heat treatment and hot isostatic pressing on the microstructure and mechanical properties of Inconel 625 alloy processed by laser powder bed fusion, Mater. Sci. Eng. A. 689 (2017) 1-10.
[30] S. Bahl, S. Mishra, K.U. Yazar, I.R. Kola, K. Chatterjee, S. Suwas, Non-equilibrium microstructure, crystallographic texture and morphological texture synergistically result in unusual mechanical properties of 3D printed 316L stainless steel, Addit. Manuf. 28 (2019) 65-77.
[31] B. AlMangour, D. Grzesiak, J.-M. Yang, Rapid fabrication of bulk-form TiB2/316L stainless steel nanocomposites with novel reinforcement architecture and improved performance by selective laser melting, J. Alloy. Compd. 680 (2016) 480-493.
[32] B. Richter, N. Blanke, C. Werner, F. Vollertsen, F.E. Pfefferkorn, Effect of initial surface features on laser polishing of Co-Cr-Mo alloy made by powder-bed fusion, Jom 71(3) (2019) 912-919.
[33] C.-S. Chang, T.-H. Chen, T.-C. Li, S.-L. Lin, S.-H. Liu, J.-F. Lin, Influence of laser beam fluence on surface quality, microstructure, mechanical properties, and tribological results for laser polishing of SKD61 tool steel, J. Mater. Process. Technol. 229 (2016) 22-35.
[34] M. Zhang, Y. Yang, C. Song, Y. Bai, Z. Xiao, An investigation into the aging behavior of CoCrMo alloys fabricated by selective laser melting, J. Alloy. Compd. 750 (2018) 878-886.
[35] W.M. Tucho, V.H. Lysne, H. Austbø, A. Sjolyst-Kverneland, V. Hansen, Investigation of effects of process parameters on microstructure and hardness of SLM manufactured SS316L, J. Alloy. Compd. 740 (2018) 910-925.
[36] S. Li, Q. Wei, Y. Shi, Z. Zhu, D. Zhang, Microstructure characteristics of Inconel 625 superalloy manufactured by selective laser melting, J. Mater. Sci. Technol. 31(9) (2015) 946-952.
[37] F. Zhihao, L. Libin, C. Longfei, G. Yingchun, Laser polishing of additive manufactured superalloy, Procedia CIRP 71 (2018) 150-154.
[38] K.C. Yung, T.Y. Xiao, H.S. Choy, W.J. Wang, Z.X. Cai, Laser polishing of additive manufactured CoCr alloy components with complex surface geometry, J. Mater. Process. Technol. 262 (2018) 53-64.
[39] A. Lamikiz, J.A. Sanchez, L.N.L. de Lacalle, J.L. Arana, Laser polishing of parts built up by

selective laser sintering, Int. J. Mach. Tool Manu. 47(12-13) (2007) 2040-2050.
[40] S. Wu, B. Ghaffari, E. Hetrick, M. Li, Q. Liu, Z. Jia, Thermo-mechanically affected zone in AA6111 resistance spot welds, J. Mater. Process. Technol. 249 463-470.
[41] S.-n. Wu, B. Ghaffari, E. Hetrick, M. Li, Z.-h. Jia, Q. Liu, Microstructure characterization and quasi-static failure behavior of resistance spot welds of AA6111-T4 aluminum alloy, T. Nonferr. Metal. Soc. 24(12) (2014) 3879-3885.
[42] A. Ahmadi, M.R. Toroghinejad, A. Najafizadeh, Evaluation of microstructure and mechanical properties of Al/Al2O3/SiC hybrid composite fabricated by accumulative roll bonding process, Mater. Des. 53 (2014) 13-19.
[43] Z. Hamouche-Hadjem, T. Auger, I. Guillot, D. Gorse, Susceptibility to LME of 316L and T91 steels by LBE: Effect of strain rate, J. Nucl. Mater. 376(3) (2008) 317-321.
[44] T.S. Srivatsan, S. Vasudevan, L. Park, The tensile deformation and fracture behavior of friction stir welded aluminum alloy 2024, Mater. Sci. Eng. A. 466(1-2) (2007) 235-245.
[45] Y. Zhang, J. Lu, K. Luo, Mechanical properties of AISI 304 SS and its welded joint subjected to laser shock processing, Laser Shock Processing of FCC Metals, Springer 2013, 113-135.
[46] S. Gencalp Irizalp, N. Saklakoglu, High strength and high ductility behavior of 6061-T6 alloy after laser shock processing, Opt. Laser Eng. 77 (2016) 183-190.
[47] T.S. Srivatsan, S. Vasudevan, L. Park, The tensile deformation and fracture behavior of friction stir welded aluminum alloy 2024, Mater. Sci. Eng. A. 466(1) (2007) 235-245.
[48] S.G. Irizalp, N. Saklakoglu, High strength and high ductility behavior of 6061-T6 alloy after laser shock processing, Opt. Laser Eng. 77 (2016) 183-190.
[49] J. Sun, B. Xu, Z. Yang, H. Zhou, J. Han, Y. Wu, D. Song, Y. Yuan, X. Zhuo, H. Liu, A. Ma, Achieving excellent ductility in high-strength Mg-10.6Gd-2 Ag alloy via equal channel angular pressing, J. Alloy. Compd. 817 (2020) 152688.
[50] X.C. Liu, H.W. Zhang, K. Lu, Strain-induced ultrahard and ultrastable nanolaminated structure in nickel, Science 342(6156) (2013) 337-40.
[51] H.W. Zhang, K. Lu, R. Pippan, X. Huang, N. Hansen, Enhancement of strength and stability of nanostructured Ni by small amounts of solutes, Scr. Mater. 65(6) (2011) 481-484.
[52] D.A. Hughes, N. Hansen, Microstructure and strength of nickel at large strains, Acta Mater. 48(11) (2000) 2985-3004.